nature physics

LETTERS

https://doi.org/10.1038/s41567-021-01341-w

Check for updates

Imaging phonon-mediated hydrodynamic flow in WTe_2

Uri Vool[1,2,8], Assaf Hamo[2,8], Georgios Varnavides[3,4,5,8]✉, Yaxian Wang[3,8], Tony X. Zhou[2,3,5], Nitesh Kumar[6], Yuliya Dovzhenko[2], Ziwei Qiu[2,3], Christina A. C. Garcia[3], Andrew T. Pierce[2], Johannes Gooth[2,6,7], Polina Anikeeva[4,5], Claudia Felser[3,6], Prineha Narang[3]✉ and Amir Yacoby[2,3]✉

In the presence of interactions, electrons in condensed-matter systems can behave hydrodynamically, exhibiting phenomena associated with classical fluids, such as vortices and Poiseuille flow[1–3]. In most conductors, electron–electron interactions are minimized by screening effects, hindering the search for hydrodynamic materials; however, recently, a class of semimetals has been reported to exhibit prominent interactions[4,5]. Here we study the current flow in the layered semimetal tungsten ditelluride by imaging the local magnetic field using a nitrogen-vacancy defect in a diamond. We image the spatial current profile within three-dimensional tungsten ditelluride and find that it exhibits non-uniform current density, indicating hydrodynamic flow. Our temperature-resolved current profile measurements reveal a non-monotonic temperature dependence, with the strongest hydrodynamic effects at approximately 20 K. We also report ab initio calculations showing that electron–electron interactions are not explained by the Coulomb interaction alone, but are predominantly mediated by phonons. This provides a promising avenue in the search for hydrodynamic flow and prominent electron interactions in high-carrier-density materials.

When microscopic scattering processes in condensed matter systems conserve momentum, electrons flow collectively—akin to a fluid—deviating substantially from the expected diffusive flow of a Fermi liquid. This behaviour, termed hydrodynamic electron flow, has been reported in transport measurements in (Al,Ga)As (ref. [6]), graphene[7–9], $PdCoO_2$ (ref. [4]) and WP_2 (ref. [5]). Even when momentum is conserved, the presence of boundaries does not need to respect this conservation, leading to a distinct spatial signature when current flows along a channel, known as Poiseuille flow. The resulting current profile is characterized by enhanced flow in the centre of the channel and reduced flow along the edges, as recently shown by spatially resolved measurements in graphene[10–12]. In bulk hydrodynamically reported materials (such as $PdCoO_2$ (ref. [4]) and WP_2 (ref. [5])), however, large carrier density presents unsolved mysteries regarding the microscopic origins of hydrodynamics.

Tungsten ditelluride (WTe_2) is a layered semimetal that has stirred interest in recent years as part of a new class of quantum materials. The bulk crystal exhibits large magnetoresistance[13] and pressure-driven superconductivity[14,15], and has been predicted[16] and observed[17–20] to be a type-II Weyl semimetal. In the monolayer, WTe_2 can be electrostatically gated into a quantum spin Hall insulator[21] or a superconductor[22,23]. These effects are due to the rich band structure of the material, its high conductance (carrier mean free path as long as 12 μm (ref. [24])) and substantial electron–electron interactions. Since momentum is conserved during electron–electron interactions, spatially resolved measurements of hydrodynamic flow in WTe_2 are uniquely positioned to probe interactions in the material.

In this Letter, we present the spatial profile of current flowing in a WTe_2 flake and show it is consistent with hydrodynamic flow; this is the first observation of a non-uniform current profile in a three-dimensional (3D) material. Moreover, this is a high-carrier-density material in which direct Coulomb-mediated electron–electron scattering is expected to be screened, making the observation of hydrodynamic behaviour surprising. Importantly, we find that the hydrodynamic character of the current strongly and non-monotonically depends on the temperature. From an independent first-principles investigation—which includes interactions that have so far been overlooked in the search for hydrodynamic candidates, namely, phonon-mediated electron–electron scattering[25,26]—we show that unlike Coulomb scattering, this dictates electron dynamics in WTe_2. Using these first-principles scattering rates as the input to the spatially resolved Boltzmann transport equation, we predict the hydrodynamic current density profiles that capture the non-monotonic temperature dependence. The combination of experiment and theory enables us to extract the characteristic length scale of electron–electron interactions in WTe_2, providing strong evidence for phonon-mediated hydrodynamics.

Td-WTe_2 crystallizes in the orthorhombic lattice (space group $Pmn2_1$), with two layers in the unit cell bonded by weak van der Waals interactions along the crystallographic $\hat{c}$ axis, as shown in Fig. 1a. The semimetal is charge-compensated[24] (Fig. 1b) by the WTe_2 Fermi surface with the electron (hole) pockets displayed in blue (red). We exfoliate a WTe_2 flake with a thickness of ~60 nm, cleaved along its crystallographic $\hat{a}$ axis. To image the current flow in WTe_2, we use a scanning probe based on a nitrogen-vacancy (NV) defect in a diamond[27–30], an atomic-size quantum magnetometer.

[1]John Harvard Distinguished Science Fellows Program, Harvard University, Cambridge, MA, USA. [2]Department of Physics, Harvard University, Cambridge, MA, USA. [3]Harvard John A. Paulson School of Engineering and Applied Sciences, Harvard University, Cambridge, MA, USA. [4]Department of Materials Science and Engineering, Massachusetts Institute of Technology, Cambridge, MA, USA. [5]Research Laboratory of Electronics, Massachusetts Institute of Technology, Cambridge, MA, USA. [6]Max-Planck-Institut für Chemische Physik fester Stoffe, Dresden, Germany. [7]Institut für Festkörper- und Materialphysik, Technische Universität Dresden, Dresden, Germany. [8]These authors contributed equally: Uri Vool, Assaf Hamo, Georgios Varnavides, Yaxian Wang. ✉e-mail: gvarnavi@g.harvard.edu; prineha@seas.harvard.edu; yacoby@g.harvard.edu

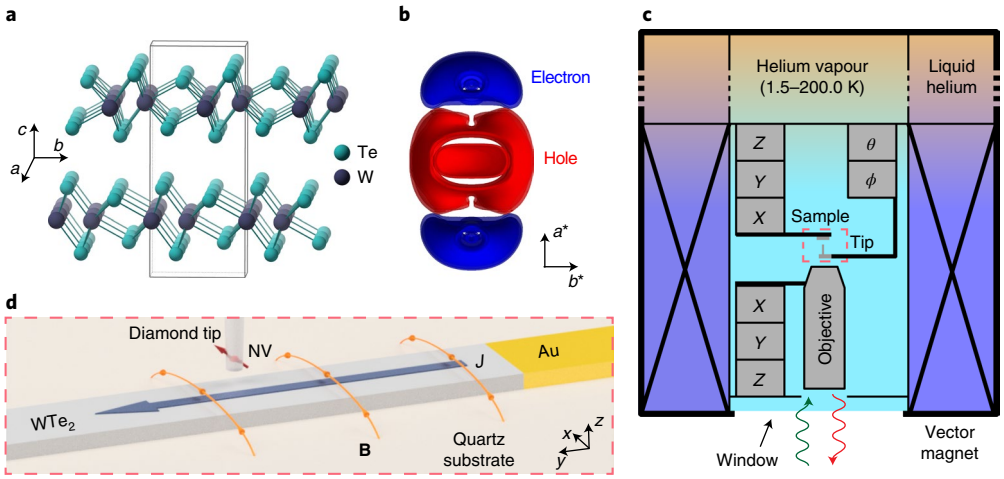

Fig. 1 | Device and experimental setup. a, Crystal structure highlighting the layered structure of WTe_2. **b**, Calculated Fermi surface for the WTe_2 lattice, with compensated electron (blue) and hole (red) pockets. **c**, A scanning magnetometry microscope mounted in a flow cryostat. The outer layer is filled with liquid helium and houses the vector magnet. A needle valve connects this bath to the central chamber, allowing the flow of helium vapour into it to control the temperature by balancing the flow rate and heating. The microscope consists of a diamond tip with an NV defect in contact with the sample, which can be moved by piezoelectric controllers along the *X*, Y and *Z* directions. The diamond tip is attached to goniometers that allow for θ and φ angle control (Methods). The bottom of the cryostat has a window for optical access, allowing us to measure the NV defect's spin state. The objective, which focuses light on the defect, can also be moved. **d**, A close-up of the diamond tip with the NV defect and WTe_2 flake. Electric current with density *J* is flowing through the flake, generating a magnetic field that is measured by the NV.

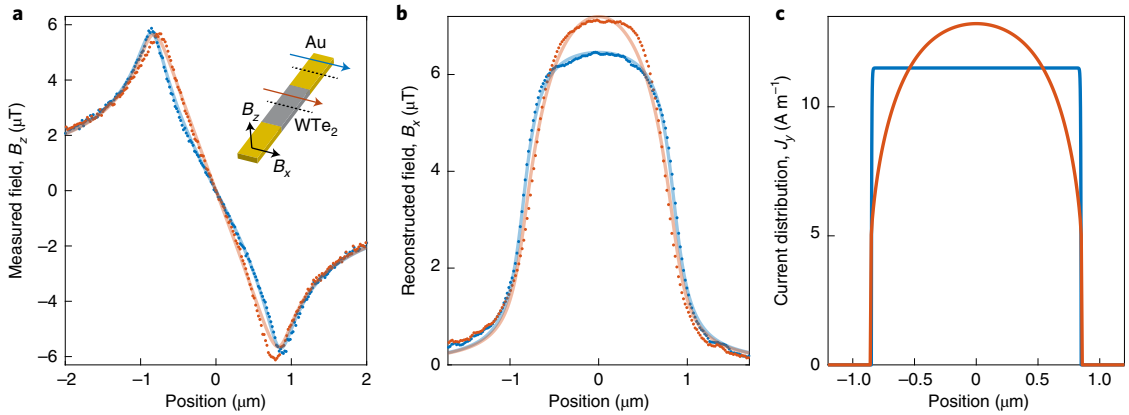

Fig. 2 | Comparison of current flow profiles in WTe_2 and gold. a, B_z magnetic field, measured by the NV sensor in a 1D scan across a channel with width $W = 1.7$ μm. The blue and orange markers show measurements along the gold contact and WTe_2 device, respectively, normalized to have a total current $I_{tot} = 20$ μA. The blue and orange lines correspond to the expected B_z field generated by the currents in **c** at a height of $h = 140$ nm measured between the NV and middle of the WTe_2 flake. The WTe_2 and gold data were taken at 20 K and 90 K, respectively, with the gold measurements showing negligible temperature dependence (Supplementary Section 3). **b**, Reconstruction of the B_x field along the scan, from the data shown in **a** for the corresponding blue and orange markers. The blue and orange lines correspond to the expected B_x field generated by the currents in **c**. Note that there is an asymmetry at the edges of the sample, with both curves appearing above the expected values on the left and below them on the right. This is probably due to an angle mismatch of 1° of our NV sensor. The lack of mirror symmetry pronounced in the middle of the channel probably reflects the true current distribution. The source of this asymmetry is currently unknown. **c**, Theoretical current distributions along a channel with width $W = 1.7$ μm and total current $I_{tot} = 20$ μA. The blue line shows a uniform profile, expected for diffusive flow. The orange line shows a curved current profile with flow enhanced in the centre of the channel and reduced along the edges (see the discussion in Fig. 4 for more details on the profile).

The NV is sensitive to the magnetic field parallel to its crystal axis through the Zeeman effect, and our experiments take advantage of the long coherence time of the NV to perform echo magnetometry and achieve magnetic sensitivity of ~10 nT (Methods and Supplementary Sections 1 and 2). The unique custom-built cryostat and scanning system used in this study, allowing imaging at variable temperatures, is schematically shown in Fig. 1c. Figure 1d shows a close-up of the diamond tip with the NV defect above the WTe_2 sample. At each tip location, the NV sensor detects the magnetic field generated by the current flowing along the sample. In our notation, the current is flowing along the $\hat{y}$ axis, generating a non-zero magnetic field in the $\hat{x}$–$\hat{z}$ plane. The NV defect axis is oriented along the $\hat{y}$–$\hat{z}$ plane, and therefore, sensitivity exists only for the $\hat{z}$ component of the magnetic field.

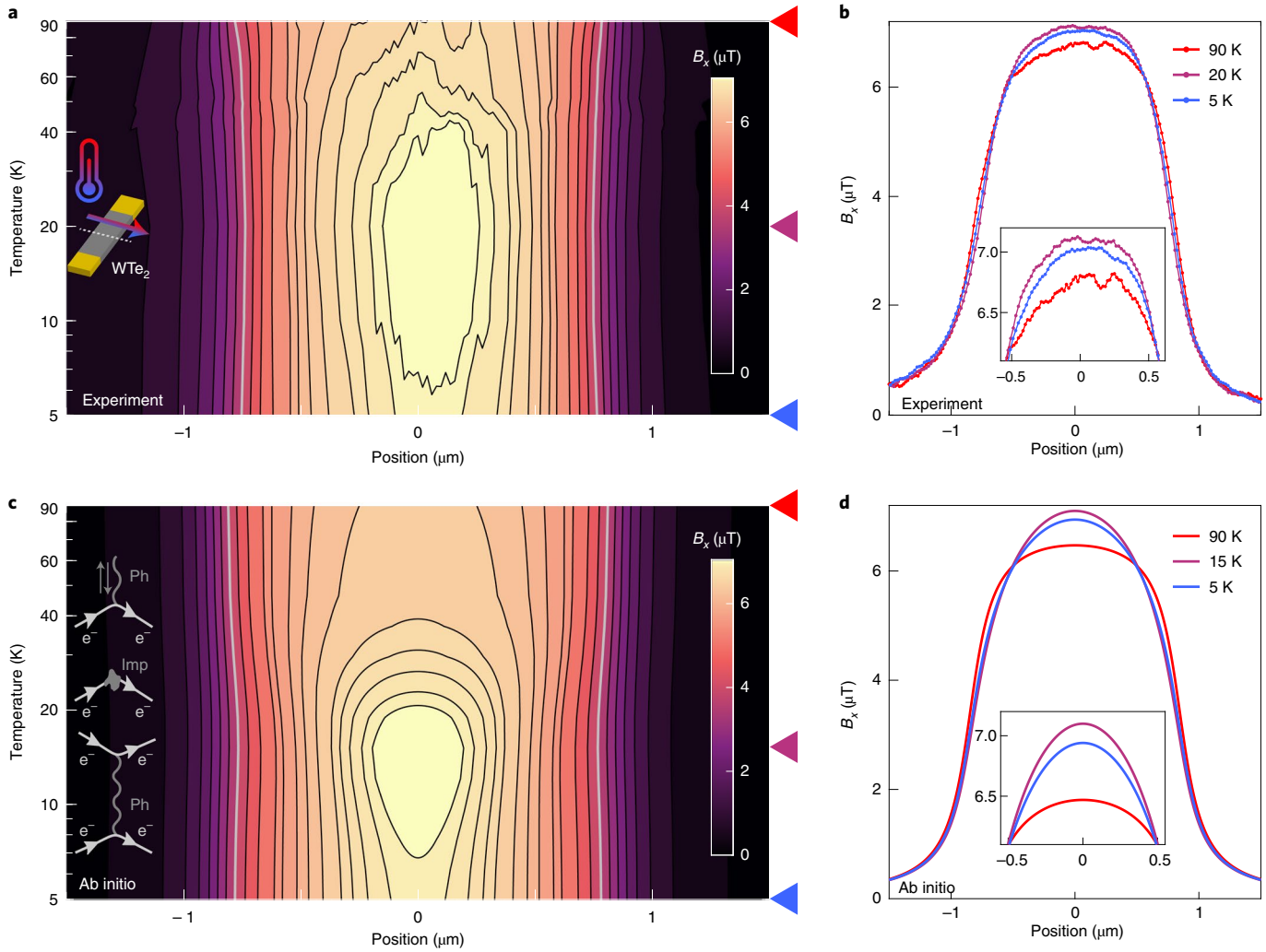

Fig. 3 | Temperature-dependent magnetic field profiles. a, Contour plot of the magnetic field profile B_x across the WTe_2 device ($\hat{x}$ axis) at different temperatures ($\hat{y}$ axis). The scans were taken along the same y position to isolate the effects of temperature on current flow (Supplementary Section 4). The contour at $B_x = 4\,\mu T$ is highlighted in grey to show the narrowest profile appears between 10 K and 20 K, where the peak height is also maximum. **b**, Three linecuts of **a** taken at 90 K, 20 K and 5 K as indicated by the respective arrows. The inset shows a zoomed-in image of the peak of the profiles. The profile at 20 K, also shown in orange in Fig. 2c, is both the narrowest and has the highest peak value. **c**, Contour plot of the magnetic field profiles obtained from numerical transport calculations using ab initio scattering rate inputs for electron–electron and electron–phonon interactions, and assuming an electron–impurity mean free path of 1.9 μm. Theory captures the non-monotonic temperature dependence, peaking at around 15 K. The corresponding Feynman diagrams are schematically shown in the inset. **d**, Three linecuts of **c** taken at 90 K, 15 K and 5 K, showing quantitative agreement with the experimental data in **b**. The inset shows a zoomed-in image of the peak of the profiles.

In Fig. 2a, we present the $\hat{z}$ component of the magnetic field (B_z) measured by our NV tip scanning along two one-dimensional (1D) linescans along the $\hat{x}$ axis, one taken above a gold (Au) contact (blue markers) and the other taken above our WTe_2 sample (orange markers). Both measurements correspond to a channel width of $W = 1.7\,\mu m$ and total current $I_{tot} = 20\,\mu A$, and were taken at a tip height of $h = 140\,nm$ measured between the NV and middle of the WTe_2 flake (Supplementary Section 7). We observe noticeable differences between the two scans, with the WTe_2 measurement showing a sharper slope in the centre of the channel and an inward shift of the extreme positions. Such differences are discernible due to the high signal-to-noise ratio of our measurement (Supplementary Section 2). To visualize the difference in the underlying current profile, we obtain the $\hat{x}$ component of the magnetic field (B_x) by Fourier reconstruction[31] of the data shown in Fig. 2a (Supplementary Section 8). This is shown by the blue and orange markers in Fig. 2b, with the WTe_2 measurement indicating enhanced current density in the centre and reduced density along the edges, suggestive of hydrodynamic flow. These observations can be made more quantitative by examining two theoretical examples of current distributions, as shown in Fig. 2c. The blue line corresponds to uniform flow, where electron–electron interactions play a negligible role—as expected for diffusive behaviour. The orange line shows a non-diffusive current distribution whose quantitative details will be discussed below. The blue and orange lines shown in Fig. 2a,b are the calculated B_z and B_x values for the corresponding profiles shown in Fig. 2c. The good agreement with experiment confirms that the current flow in gold is indeed uniform. Notice that the finite height offset of the NV tip convolves the current distributions for both gold and WTe_2, resulting in a non-flat B_x profile even for a fully diffusive current distribution. By contrast, the flow in WTe_2 significantly deviates from diffusive flow, even after taking the finite height into account.

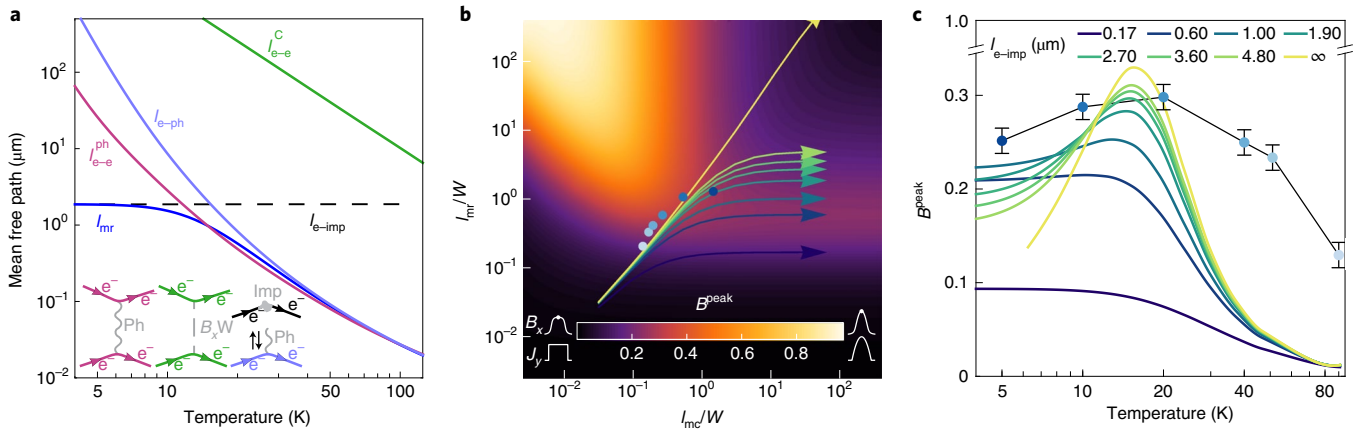

Fig. 4 | Ab initio lifetimes and Boltzmann transport equation. a, Temperature-dependent ab initio electron mean free paths for WTe_2, obtained using density functional theory (Methods). We consider electron–phonon scattering (l_{e-ph}), electron–impurity scattering (l_{e-imp}), electron–electron scattering mediated by a screened Coulomb interaction (l^{C}_{e-e}) and electron–electron scattering mediated by a virtual phonon (l^{ph}_{e-e}). The corresponding Feynman diagrams are schematically shown in the inset. The overall momentum-relaxing electron mean free path (l_{mr}) is calculated using Matthiessen's rule. **b**, Normalized B_x magnetic field phase diagram, extracted from the current profiles computed using the Boltzmann transport equation allowing for momentum-conserving ($\hat{x}$ axis) and momentum-relaxing ($\hat{y}$ axis) interactions[4,6]. The colour corresponds to the magnetic field B_x in the centre of the channel, normalized to be 0 for uniform flow and 1 for perfect parabolic Poiseuille flow, as highlighted by the inset. Overlaid arrows indicate the decreasing-temperature trajectories predicted ab initio in **a** for various values of the electron–impurity mean free path (l_{e-imp}) following the legend in **c**. Points correspond to fits of the magnetic field profile to the experimental data at different temperatures, following the colours in **c**. **c**, One-dimensional linecuts along the arrow trajectories in **b**, indicating the ab initio theory captures the non-monotonic temperature dependence of the observed hydrodynamic phenomena for l_{e-imp} larger than 1 μm, after which the position of the peak at approximately 15 K remains unchanged. The points correspond to experimental data at different temperatures shown in Fig. 3, with error bars signifying the measurement sensitivity.

We then apply our apparatus to probe the temperature dependence of electron interactions in WTe_2 and their influence on hydrodynamic behaviour. Figure 3a shows a contour plot of the B_x magnetic field profile across our WTe_2 sample, taken at different temperatures. The magnetic field at the centre of the channel becomes higher with lower temperature, until it peaks at 10–20 K, and then becomes lower again. Similarly, the width of the profile, highlighted by the grey contour at $B_x = 4$ μT, is also the narrowest at around 10–20 K. This non-monotonic behaviour[9] is evident in three field profiles taken at 90, 20 and 5 K (Fig. 3b). The profile at 20 K is both the narrowest and has the highest peak value, indicating that hydrodynamic effects on current flow are the maximum at this temperature.

To understand the underlying microscopic origin of hydrodynamic behaviour in WTe_2 and its non-monotonic temperature dependence, we investigate the competition of electron–electron interactions with boundary scattering and momentum-relaxing scattering against lattice vibrations and impurities in the sample. From an independent ab initio theory, we extract the temperature dependence of the different scattering mechanisms in WTe_2. These are used to solve the Boltzmann transport equation in the relaxation time approximation[4,6] to obtain the steady-state current profiles (Methods) used to extract the magnetic field profiles, which are shown as a function of temperature in Fig. 3c. The theoretical predictions capture the non-monotonic temperature dependence, with the peak (approximately 15 K) showing quantitative agreement with the experiment. Note that while the results presented in the manuscript use a circular Fermi surface assumption, relaxing this assumption does not significantly change our conclusions (Supplementary Section 9.8).

The theoretical current profiles can be generally described as a function of two non-dimensional parameters: the ratio of the momentum-relaxing and momentum-conserving processes' mean free paths to the channel width W, namely, l_{mr}/W and l_{mc}/W, respectively. Microscopically, we consider two momentum-relaxing processes, namely, electron–phonon scattering (l_{e-ph}) and electron–impurity scattering (l_{e-imp}), and two momentum-conserving processes, namely, electron–electron scattering mediated by a screened Coulomb interaction (l^{C}_{e-e}) and that by a virtual phonon (l^{ph}_{e-e}). Figure 4a shows the full temperature dependence of these mean free paths for WTe_2, given by our ab initio calculation, which include contributions from all the electron and hole pockets (Supplementary Section 13). The momentum-conserving mean free path is dominated by the phonon-mediated interaction, as l^{C}_{e-e} is at least two orders of magnitude higher than l^{ph}_{e-e} at all temperatures. In contrast, both electron–phonon and electron–impurity scattering processes contribute to the momentum-relaxing mean free path. We represent the resulting current profiles—as a function of these two non-dimensional parameters—by the normalized B_x magnetic field peak (B^{peak}) in the middle of the channel, as shown in Fig. 4b (Supplementary Section 9.6). It is instructive to identify four limits in our phase diagram: (1) in the absence of momentum-conserving events ($l_{mc} \gg W$) and numerous momentum-relaxing events ($l_{mr} \ll W$) (phase diagram in Fig. 4b, bottom right), electron flow is diffusive; (2) in the absence of both momentum-conserving and momentum-relaxing events ($l_{mc} \gg W$ and $l_{mr} \gg W$; Fig. 4b, top right), boundary effects dominate, leading to ballistic flow; (3) in the presence of numerous momentum-conserving events ($l_{mc} \ll W$) and the absence of momentum-relaxing events ($l_{mr} \gg W$; Fig. 4b, top left), electrons flow collectively and we observe hydrodynamic flow; (4) finally, in the presence of both momentum-relaxing and momentum-conserving events ($l_{mc} \ll W$ and $l_{mr} \ll W$; Fig. 4b, bottom left), the flow is momentum-'porous', and the regime is referred to as 'Ziman' hydrodynamics[32].

While Fig. 4a highlights that both l_{mr} and l_{mc} increase monotonically with decreasing temperature, Fig. 4b confirms that there exist 1D temperature trajectories that support non-monotonic behaviour. Note that even in the absence of momentum-conserving interactions (far right of the phase diagram in Fig. 4b), the current density can exhibit non-monotonic behaviour, albeit with quantitative disagreement with our experiment and ab initio calculation (Supplementary

Section 9.5). Overlaid arrows in Fig. 4b mark the decreasing temperature trajectories following the ab initio calculations in Fig. 4a, for empirical values of l_{e-imp} between 0.17 and 4.80 µm. The arrow for infinite impurity corresponds to momentum relaxation only due to electron–phonon interactions. Similarly, we can fit the experimental profiles at different temperatures to one such trajectory, shown by the overlaid points in Fig. 4b. Notice that our measurements do not comfortably fit in any of the previously identified limits, and thus, both ballistic and hydrodynamic effects contribute to the resulting current flow. The ab initio predictions agree well with experimental profiles, albeit the experimental data suggests a weaker temperature dependence and at high temperatures, theory predicts a more diffusive profile than the one measured in the experiment. This deviation may be attributed to the finite thickness of the sample, position-dependent mean free path due to sample imperfections or modification of the phonon spectrum by the presence of the quartz substrate (Supplementary Section 12). Furthermore, relaxing the circular Fermi surface assumption results in modified current density curvature that could also account for some of the discrepancies (Supplementary Section 9.8). The non-monotonic behaviour is shown more clearly in Fig. 4c, which plots these 1D trajectories for empirical values of l_{e-imp} between 0.17 and 4.80 µm (Fig. 4c). While a minimum impurity mean free path is necessary to observe non-monotonic behaviour, the location of the peak is largely independent of l_{e-imp} above this threshold. This allows us to extract a robust estimate for the electron–electron interaction length, namely, $l_{e-e}^{ph} \approx 200$ nm at 10–20 K. The ab initio calculation was performed on a fully relaxed WTe_2 lattice. When the lattice is constrained to accommodate Weyl nodes, electron–electron interactions increase, resulting in the non-monotonic behaviour peaking at approximately 8 K (Supplementary Section 11). This is in contrast with our observations, suggesting that our sample was not in the Weyl phase.

This work opens the possibility of observing hydrodynamic effects and electron interactions even in high-carrier-density materials, where direct electron–electron interactions are screened (Supplementary Section 14). The comparison of theoretical predictions and experimental observations allows us to extract a robust estimate of the electron–electron interaction length in WTe_2, an important quantity for interacting systems otherwise challenging to extract experimentally. Quantifying the magnitude of electron interactions in 3D materials could reveal the microscopic mechanisms underlying strongly interacting systems, such as high-temperature superconductors and strange metals[33,34]. While we focus on one WTe_2 crystallographic orientation in this work, our setup allows the exploration and imaging of anisotropic hydrodynamic flows in 3D crystals. By studying different geometries and orientations of such anisotropic materials, future work will permit the observations of non-classical fluid behaviour such as steady-state vortices, coupling of fluid stress to vorticity and 3D Hall viscosity[35].

Online content

Any methods, additional references, Nature Research reporting summaries, source data, extended data, supplementary information, acknowledgements, peer review information; details of author contributions and competing interests; and statements of data and code availability are available at https://doi.org/10.1038/s41567-021-01341-w.

Received: 20 December 2020; Accepted: 23 July 2021;
Published online: 16 September 2021

References

1. Gurzhi, R. N. Hydrodynamic effects in solids at low temperature. *Sov. Phys. Usp.* **11**, 255–270 (1968).
2. Levitov, L. & Falkovich, G. Electron viscosity, current vortices and negative nonlocal resistance in graphene. *Nat. Phys.* **12**, 672–676 (2016).
3. Andrew, L. & Fong, K. C. Hydrodynamics of electrons in graphene. *J. Phys. Condens. Matter* **30**, 053001 (2018).
4. Moll, P. J. W., Kushwaha, P., Nandi, N., Schmidt, B. & Mackenzie, A. P. Evidence for hydrodynamic electron flow in $PdCoO_2$. *Science* **351**, 1061–1064 (2016).
5. Gooth, J. et al. Thermal and electrical signatures of a hydrodynamic electron fluid in tungsten diphosphide. *Nat. Commun.* **9**, 4093 (2018).
6. de Jong, M. J. M. & Molenkamp, L. W. Hydrodynamic electron flow in high-mobility wires. *Phys. Rev. B* **51**, 13389–13402 (1995).
7. Bandurin, D. A. et al. Negative local resistance caused by viscous electron backflow in graphene. *Science* **351**, 1055–1058 (2016).
8. Jesse, C. et al. Observation of the Dirac fluid and the breakdown of the Wiedemann–Franz law in graphene. *Science* **351**, 1058–1061 (2016).
9. Krishna Kumar, R. et al. Superballistic flow of viscous electron fluid through graphene constrictions. *Nat. Phys.* **13**, 1182–1185 (2017).
10. Sulpizio, J. A. et al. Visualizing Poiseuille flow of hydrodynamic electrons. *Nature* **576**, 75–79 (2019).
11. Ku, M. J. H. et al. Imaging viscous flow of the Dirac fluid in graphene. *Nature* **583**, 537–541 (2020).
12. Jenkins, A. et al. Imaging the breakdown of ohmic transport in graphene. Preprint at https://arxiv.org/abs/2002.05065 (2020).
13. Ali, M. N. et al. Large, non-saturating magnetoresistance in WTe_2. *Nature* **514**, 205–208 (2014).
14. Kang, D. et al. Superconductivity emerging from a suppressed large magnetoresistant state in tungsten ditelluride. *Nat. Commun.* **6**, 7804 (2015).
15. Pan, X.-C. et al. Pressure-driven dome-shaped superconductivity and electronic structural evolution in tungsten ditelluride. *Nat. Commun.* **6**, 7805 (2015).
16. Soluyanov, A. A. et al. Type-II Weyl semimetals. *Nature* **527**, 495–498 (2015).
17. Peng, L. et al. Evidence for topological type-II Weyl semimetal WTe_2. *Nat. Commun.* **8**, 2150 (2017).
18. Lin, C.-L. et al. Visualizing type-II Weyl points in tungsten ditelluride by quasiparticle interference. *ACS Nano* **11**, 11459–11465 (2017).
19. Lv, Y.-Y. et al. Experimental observation of anisotropic Adler–Bell–Jackiw anomaly in type-II Weyl semimetal $WTe_{1.98}$ crystals at the quasiclassical regime. *Phys. Rev. Lett.* **118**, 096603 (2017).
20. Sie, E. J. et al. An ultrafast symmetry switch in a Weyl semimetal. *Nature* **565**, 61–66 (2019).
21. Sanfeng, W. et al. Observation of the quantum spin Hall effect up to 100 kelvin in a monolayer crystal. *Science* **359**, 76–79 (2018).
22. Valla, F. et al. Electrically tunable low-density superconductivity in a monolayer topological insulator. *Science* **362**, 926–929 (2018).
23. Sajadi, E. et al. Gate-induced superconductivity in a monolayer topological insulator. *Science* **362**, 922–925 (2018).
24. Zhu, Z. et al. Quantum oscillations, thermoelectric coefficients, and the Fermi surface of semimetallic WTe_2. *Phys. Rev. Lett.* **114**, 176601 (2015).
25. Coulter, J., Sundararaman, R. & Narang, P. Microscopic origins of hydrodynamic transport in the type-II Weyl semimetal WP_2. *Phys. Rev. B* **98**, 115130 (2018).
26. Levchenko, A. & Schmalian, J. Transport properties of strongly coupled electron–phonon liquids. *Ann. Phys.* **419**, 168218 (2020).
27. Maletinsky, P. et al. A robust scanning diamond sensor for nanoscale imaging with single nitrogen-vacancy centres. *Nat. Nanotechnol.* **7**, 320–324 (2012).
28. Pelliccione, M. et al. Scanned probe imaging of nanoscale magnetism at cryogenic temperatures with a single-spin quantum sensor. *Nat. Nanotechnol.* **11**, 700–705 (2016).
29. Zhou, T. X., Stöhr, R. J. & Yacoby, A. Scanning diamond NV center probes compatible with conventional AFM technology. *Appl. Phys. Lett.* **111**, 163106 (2017).
30. Ling, X., Zhou, T. X., Stöhr, R. J. & Yacoby, A. Crystallographic orientation dependent reactive ion etching in single crystal diamond. *Adv. Mater.* **30**, 1705501 (2018).
31. Casola, F., van der Sar, T. & Yacoby, A. Probing condensed matter physics with magnetometry based on nitrogen-vacancy centres in diamond. *Nat. Rev. Mater.* **3**, 17088 (2018).
32. Guyer, R. A. & Krumhansl, J. A. Thermal conductivity, second sound, and phonon hydrodynamic phenomena in nonmetallic crystals. *Phys. Rev.* **148**, 778–788 (1966).
33. Hartnoll, S. A., Kovtun, P. K., Müller, M. & Sachdev, S. Theory of the Nernst effect near quantum phase transitions in condensed matter and in dyonic black holes. *Phys. Rev. B* **76**, 144502 (2007).
34. Davison, R. A., Schalm, K. & Zaanen, J. Holographic duality and the resistivity of strange metals. *Phys. Rev. B* **89**, 245116 (2014).
35. Georgios, V., Jermyn, A. S., Polina, A., Claudia, F. & Prineha, N. Electron hydrodynamics in anisotropic materials. *Nat. Commun.* **11**, 4710 (2020).

Methods

Sample details. Single crystals of WTe_2 were grown by excess Te flux. In the typical synthesis, pieces of W (99.95%, Chempur) and Te (99.9999%, Alfa Aesar) were weighed according to the stoichiometric ratio of $W_{1.8}Te_{98.2}$ (5 g) and kept in a quartz crucible. This crucible was vacuum sealed inside a quartz tube. The reaction content was heated to 1,050 °C at a rate of 100 °C h^{-1} in a programmable muffle furnace. This temperature was maintained for 10 h to get a homogeneous molten phase, after which the temperature was slowly lowered to 750 °C at a rate of 1 °C h^{-1}. At this temperature, excess molten flux was removed by centrifugation to obtain shiny plate-like single crystals of WTe_2. The high quality of the single crystal is evidenced by the high residual resistivity ratio and quantum oscillations, as shown in Extended Data Fig. 1. The total carrier density and average mobility of the bulk sample were extracted from the magnetoresistance data (at 2 K) to be 1.4×10^{20} cm^{-3} and 2.5×10^{5} cm^2 (V s)$^{-1}$, respectively (Extended Data Fig. 2). Note that the measurements were performed on a sample made from the same bulk crystal as the device used in the main text. To capture the contributions of both electron and hole carriers at higher temperature, we turn to Hall resistivity measurements using a two-band model. The extracted estimate for carrier density and mobility for holes and electrons is shown in Extended Data Fig. 3.

We exfoliated WTe_2 flakes and searched for elongated samples that maintain a constant width along a segment, allowing us to assume uniform current flow in this segment. The chosen flake was then transferred onto our quartz substrate. The flake was placed close to a gold line used for the delivery of a radio-frequency (RF) signal, necessary for manipulating the states of the NV. This RF signal required the use of an insulating substrate, as the conducting plane of a typical silicon substrate would screen the RF signal and prevent NV manipulation. After placing the flake, we patterned and evaporated gold contacts following argon ion cleaning (without breaking the vacuum). No lithographic process was performed to define the edges of our device. Extended Data Fig. 4 shows an optical image of the WTe_2 sample used for the experiments shown in Figs. 2–4. It is a 60-nm-thick, 100-μm-long flake. We scanned along a 1.7-μm-wide profile in a uniform segment of the flake (the dashed white line in Extended Data Fig. 4). The gold scan (shown as the blue line in Fig. 2b) was taken on the gold contact shown to the right of the sample in the image. The evaporated gold was also 60 nm thick to match the thickness of the WTe_2 flake.

Scanning probe details and multiple pillar probe. Our magnetic sensing experiment is based on a diamond scanning probe with an NV defect close to its surface. The design and fabrication of our probes is presented in detail in ref. [29]. However, our cryogenic setup requires a variation of this design, which is described here. Our scanning tip is glued to a standard quartz tuning fork, and monitoring of the tuning fork frequency allows us to maintain a constant height above our sample during the scan. Extended Data Fig. 5a shows the two legs of our tuning fork, and a quartz rod glued to one of the legs. The quartz rod itself is glued to a 50-μm-thick, 50-μm-wide and 125-μm-long diamond cube. A close-up of the diamond is shown in Extended Data Fig. 5b, and the 3 μm etched diamond pillar can be seen. Our NV defect is located approximately 20 nm away from the pillar edge. Notice that our tuning fork is positioned horizontally, as opposed to the vertical position, which is common in atomic force microscopy systems. This is due to size restrictions in our setup, imposed by the short (700 μm) focal length of our objective. In the configuration described above, our diamond tip is in contact with the measured surface. This method was problematic for certain materials (including WTe_2 measured by us), as the tip was damaging the surface of the material during the scan. In addition, the material accumulated on the tip itself, which reduced the optical contrast of the NV and compromised our measurement. To overcome this problem, we fabricated diamond tips with several pillars so that one pillar is used for atomic force microscopy contact, while another is used for magnetic sensing. This technique uses the angle control available in our setup due to goniometric motors (notice the motors labelled ϕ and θ in Fig. 2a), as by tuning the angle, we can control which tip will be in contact as well as the height of the scanning tip above the sample. In this study, the tip height was chosen as a safety precaution as the damage of a crash can be severe to both sample and tip. Extended Data Fig. 6a shows a sketch of our scanning method, where one pillar is in contact with the substrate (so that it does not damage the device), while another is used for scanning the sample. The angle θ of the diamond tip is used to tune the height of the NV above the sample. Extended Data Fig. 6b shows an optical image of such a multiple pillar diamond with seven pillars in a row. The outer contact pillars are made to be thicker (approximately 800 nm diameter on the edge) so they are optimized for durability on contact. The central pillars are thin (300–400 nm diameter in the middle) as they contain one NV defect per pillar on average, and they are optimized for optical waveguiding.

Echo magnetometry measurements. Our magnetic field data is measured using an echo magnetometry sequence on the NV for time $\tau = 21$ μs. A current of 19 μA is applied through the device during this sequence, alternating in direction between the two halves of the sequence. To extract the phase, we repeat this experiment with four different final π/2 pulse options: π/2 pulse around the x axis, π/2 pulse around the y axis, $-\pi/2$ pulse around the x axis and $-\pi/2$ pulse around the y axis. The phase can the be extracted from the measurements by

$$\varphi = \arctan\left(\frac{M_{x\pi/2} - M_{x-\pi/2}}{M_{y-\pi/2} - M_{y\pi/2}}\right), \tag{1}$$

where $M_{x\pi/2}$ is the measurement following the π/2 pulse around the x axis and the others are defined in a similar manner. Supplementary Section 1 provides more information.

Ab initio calculations of different scattering mechanisms. WTe_2 is a semimetal with considerable density of states at the Fermi level, where the electrons mainly scatter against other electrons and phonons. Here we consider four microscopic electron scattering events in WTe_2: momentum-conserving electron–electron (e–e) scattering mediated by Coulomb screening (τ_{ee}^{W}) and that by a phonon (τ_{ee}^{PH}), in addition to the momentum-relaxing electron–phonon (e–ph) scattering (τ_{eph}) and electron–impurity (e–imp) scattering (τ_{imp}) (Fig. 4). Details of the methodology can be found in earlier works[25,36–39] and a similar study on type-II Weyl semimetal WP_2 has successfully revealed the electron scattering microscopics[25].

Electron–phonon scattering. For an electron with energy $\varepsilon_{n\mathbf{k}}$ (with band index n and wavevector $\mathbf{k}$) scattered by a phonon of energy $\omega_{\mathbf{q}\nu}$ (momentum $\mathbf{q}$ and branch index ν), the electron final state has momentum $\mathbf{k}+\mathbf{q}$ and energy $\varepsilon_{m\mathbf{k}+\mathbf{q}}$ (where m is the new band index). The electron–phonon scattering time (τ_{eph}) can be obtained from the electron self-energy by Fermi's golden rule as follows:

$$\begin{aligned}\tau_{eph}^{-1}(n\mathbf{k}) = {} & \tfrac{2\pi}{\hbar}\sum_{m\nu\pm}\int_{BZ}\tfrac{d\mathbf{q}}{\Omega_{BZ}}|g_{mn,\nu}(\mathbf{k},\mathbf{q})|^2 \\ & \times\left[n_{\mathbf{q}\nu}+\tfrac{1}{2}\mp\left(\tfrac{1}{2}-f_{m\mathbf{k}+\mathbf{q}}\right)\right]\delta(\varepsilon_{n\mathbf{k}}\mp\omega_{\mathbf{k}\nu}-\varepsilon_{m\mathbf{k}+\mathbf{q}})\Big],\end{aligned} \tag{2}$$

where ħ is the reduced Planck constant, Ω_{BZ} is the Brillouin zone volume, and $f_{n\mathbf{k}}$ and $n_{\mathbf{q}\nu}$ are the Fermi–Dirac and Bose–Einstein distribution functions, respectively. The electron–phonon matrix element for a scattering vertex is given by

$$g_{mn,\nu}(\mathbf{k},\mathbf{q}) = \left(\frac{\hbar}{2m_0\omega_{\mathbf{q}\nu}}\right)^{1/2}\langle\psi_{m\mathbf{k}+\mathbf{q}}|\,\partial_{\mathbf{q}\nu}V\,|\psi_{n\mathbf{k}}\rangle\,. \tag{3}$$

Here $\langle\psi_{m\mathbf{k}+\mathbf{q}}|$ and $|\psi_{n\mathbf{k}}\rangle$ are Bloch eigenstates, m_0 is the mass of the nucleus and $\partial_{\mathbf{q}\nu}V$ is the perturbation of the self-consistent potential with respect to ion displacement associated with a phonon branch with frequency $\omega_{\mathbf{q}\nu}$. The momentum-relaxing electron scattering rates are evaluated by accounting for the change in momentum between the final and initial states based on their relative scattering angle as follows:

$$\begin{aligned}\left(\tau_{eph}^{mr}(n\mathbf{k})\right)^{-1} = {} & \tfrac{2\pi}{\hbar}\sum_{m\nu}\int_{BZ}\tfrac{d\mathbf{q}}{\Omega_{BZ}}|g_{mn,\nu}(\mathbf{k},\mathbf{q})|^2 \\ & \times\left[n_{\mathbf{q}\nu}+\tfrac{1}{2}\mp\left(\tfrac{1}{2}-f_{m\mathbf{k}+\mathbf{q}}\right)\right]\delta(\varepsilon_{n\mathbf{k}}\mp\omega_{\mathbf{q}\nu}-\varepsilon_{m\mathbf{k}+\mathbf{q}}) \\ & \times\left(1-\tfrac{v_{n\mathbf{k}}\cdot v_{m\mathbf{k}+\mathbf{q}}}{|v_{n\mathbf{k}}||v_{m\mathbf{k}+\mathbf{q}}|}\right),\end{aligned} \tag{4}$$

where $v_{n\mathbf{k}}$ is the group velocity. We calculate the temperature-dependent momentum-relaxing τ_{mr} by taking a Fermi-surface average weighted by $|v_{n\mathbf{k}}|^2$ and the energy derivative of the Fermi occupation for transport properties as follows:

$$\tau_{eph}^{mr} = \frac{\int_{BZ}\frac{d\mathbf{k}}{(2\pi)^3}\sum_n\frac{\partial f_{n\mathbf{k}}}{\partial\varepsilon_{n\mathbf{k}}}|v_{n\mathbf{k}}|^2\tau_{eph}^{mr}(n\mathbf{k})}{\int_{BZ}\frac{d\mathbf{k}}{(2\pi)^3}\sum_n\frac{\partial f_{n\mathbf{k}}}{\partial\varepsilon_{n\mathbf{k}}}|v_{n\mathbf{k}}|^2}. \tag{5}$$

Phonon-mediated electron–electron scattering. The electron–electron scattering rate mediated by a virtual phonon can be estimated within the random phase approximation by

$$\begin{aligned}(\tau_{ee}^{PH})^{-1} = {} & \tfrac{\pi\hbar^2}{2k_BTg(\varepsilon_F)}\sum_\nu\int\tfrac{\Omega_{BZ}d\mathbf{q}}{(2\pi)^3}G_{\mathbf{q}\nu}^2 \\ & \times\int_{-\infty}^{+\infty}\tfrac{\omega^2d\omega}{|\bar{\omega}_{\mathbf{q}\nu}-\omega|^2\sinh^2\frac{\hbar\omega}{2k_BT}}.\end{aligned} \tag{6}$$

Here, k_B is the Boltzmann constant, T is the temperature in kelvin, $g(\varepsilon_F)$ is the density of states at the Fermi level and $\bar{\omega}_{\mathbf{q}\nu} = \omega_{\mathbf{q}\nu}(1+i\pi G_{\mathbf{q}\nu})$ is the complex phonon frequency corrected by the electron–phonon scattering linewidth. Each phonon mode is weighed within the Eliashberg spectral function by

$$\begin{aligned}G_{\mathbf{q}\nu} = {} & \sum_{mn}\int\tfrac{\Omega_{BZ}d\mathbf{k}}{(2\pi)^3}|g_{mn,\nu}(\mathbf{k},\mathbf{q})|^2 \\ & \times\delta(\varepsilon_{n\mathbf{k}}-\varepsilon_F)\delta(\varepsilon_{m\mathbf{k}+\mathbf{q}}-\varepsilon_F).\end{aligned} \tag{7}$$

Coulomb-screening-mediated electron–electron scattering. The Coulomb-mediated electron–electron scattering rate is obtained by the imaginary part of the quasiparticle self-energy at each momentum and state ($\mathrm{Im}\Sigma_{n\mathbf{k}}(n\mathbf{k})$) as

$$\tau_{ee}^{-1}(n\mathbf{k}) = \frac{2\pi}{\hbar}\int_{BZ}\frac{d\mathbf{k}'}{(2\pi)^3}\sum_{n'}\sum_{\mathbf{GG}'}\tilde{\rho}_{n'\mathbf{k}',n\mathbf{k}}(\mathbf{G})\tilde{\rho}^{*}_{n'\mathbf{k}',n\mathbf{k}}(\mathbf{G}') \times \frac{4\pi e^2}{|\mathbf{k}'-\mathbf{k}+\mathbf{G}|^2}\mathrm{Im}[\epsilon^{-1}_{\mathbf{GG}'}(\mathbf{k}'-\mathbf{k},\varepsilon_{n,\mathbf{k}}-\varepsilon_{n'\mathbf{k}'})], \quad (8)$$

where $\tilde{\rho}_{n'\mathbf{k}',n\mathbf{k}}(\mathbf{G})$ is the plane-wave expansion of the product density $\sum_{\sigma} u^{\sigma *}_{n'\mathbf{k}'}(\mathbf{r})u^{\sigma}_{n\mathbf{k}}(\mathbf{r})$ of the Bloch functions with reciprocal lattice vectors $\mathbf{G}$, and $\epsilon^{-1}_{\mathbf{GG}'}(\mathbf{k}'-\mathbf{k},\varepsilon_{n,\mathbf{k}}-\varepsilon_{n'\mathbf{k}'})$ is the microscopic dielectric function in a plane-wave basis calculated within the random phase approximation.

We then utilize the analytical relation of τ_{ee} with dependence on temperature according to the conventional Fermi liquid theory since WTe_2 has a considerable density of states at ε_F. Here the electron–electron scattering rate grows quadratically away from the Fermi energy and with temperature as

$$\tau_{ee}^{-1}(\varepsilon, T) \approx \frac{D_e}{\hbar}[(\varepsilon-\varepsilon_F)^2 + (\pi k_B T)^2]. \quad (9)$$

We obtain τ_{ee}^{-1} by fitting all the self-energies in the entire Brillouin zone for all the energy bands at 298 K, extracting the constant of proportionality, D_e, and then adding the temperature dependence[36].

Finally, taking into account the impurity scattering, the overall momentum-relaxing mean free path (l_{mr}) and momentum-conserving mean free path (l_{mc}) are estimated by Matthiessen's rule as follows:

$$l_{mr} = \frac{v_F}{(\tau^{mr}_{eph})^{-1}+(\tau_{imp})^{-1}}, \quad l_{mc} = \frac{v_F}{(\tau^{PH}_{ee})^{-1}+(\tau^{W}_{ee})^{-1}}, \quad (10)$$

where v_F is the Fermi-surface averaged velocity and τ_{imp} is the impurity scattering time that does not have temperature dependence but varies in different samples.

Boltzmann transport equation calculations. We numerically solve the electronic Boltzmann transport equation in the presence of momentum-conserving scattering. In the steady state, the evolution of the distribution function $f(\mathbf{r},\mathbf{k})$ for non-equilibrium electrons in the neighbourhood of position $\mathbf{r}$ with wavevector $\mathbf{k}$ is given by

$$\mathbf{v}_{\mathbf{k}}\cdot\nabla_{\mathbf{r}}f(\mathbf{r},\mathbf{k}) + e\mathbf{E}\cdot\nabla_{\mathbf{k}}f(\mathbf{r},\mathbf{k}) = \Gamma[f], \quad (11)$$

where ∇ is the gradient operator, $\mathbf{v}_{\mathbf{k}}$ is the electron group velocity and $\Gamma[f]$ is the collision integral. We consider flow through a 2D channel ($\boldsymbol{r}=(x,y)$) of width W, for a circular Fermi surface ($\mathbf{v}=v_F(\cos\theta,\sin\theta)$), at the relaxation time approximation level. Under these approximations, we linearize equation (11), yielding an integro-differential equation in terms of an 'effective' mean free path, l_{eff} (ref. [6]):

$$\sin(\theta)\partial_y l_{eff}(y,\theta) + \frac{l_{eff}(y,\theta)}{l} = 1 + \frac{\tilde{l}_{eff}}{l_{mc}}, \quad (12)$$

where we use Mathhiessen's rule $l^{-1} = l_{mc}^{-1} + l_{mr}^{-1}$ to combine the depopulation of electronic states with a combined mean free path l. Note our treatment implicitly assumes a single electronic carrier, neglecting transport effects due to electron–hole collisions[40]. We justify this assumption by computing the relative contributions of scattering between different charge carriers, and show that they can be safely ignored (Supplementary Section 13). Momentum conservation is accounted for by the last term, which defines the 'average' mean free path $\tilde{l}_{eff}(y)$ and is directly proportional to current density, $j_x(y)$:

$$\tilde{l}_{eff}(y) = \int_0^{2\pi}\frac{d\theta}{\pi}\cos^2(\theta)l_{eff}(y,\theta), \quad (13)$$

$$j_x(y) = \left(\frac{m}{\pi\hbar^2}\right)\varepsilon_F e^2\frac{E_x}{mv_F}\tilde{l}_{eff}(y), \quad (14)$$

where m is the electronic effective mass, E_x is the electric field component in the x direction and v_F is the Fermi velocity. Equation (12) is numerically solved by transforming it into a Fredholm integral equation of the second kind[6]:

$$\tilde{l}_{eff}(y) - \frac{1}{l_{mc}}\int_{-W/2}^{W/2}dy' K(y,y')\tilde{l}_{eff}(y') = \tilde{l}^{(0)}_{eff}(y), \quad (15)$$

$$\tilde{l}^{(0)}_{eff}(y) = l - \frac{2l}{\pi}\int_0^{\pi/2}d\phi\cos^2(\phi) \times\left\{\exp\left(-\frac{W/2+y}{l\sin(\phi)}\right)+\exp\left(-\frac{W/2-y}{l\sin(\phi)}\right)\right\}, \quad (16)$$

$$K(y,y') := \frac{2}{\pi}\int_0^{\pi/2}d\phi\frac{\cos^2(\phi)}{\sin(\phi)}\exp\left(-\frac{|y-y'|}{l\sin(\phi)}\right). \quad (17)$$

To ensure numerical stability across a wide range of $l_{mr(mc)}/W$ values, we solve this using the modified quadrature method[41].

Data availability

Data for figures that support the manuscript are available at https://doi.org/10.7910/DVN/ULRIZG. All other data that support the findings of this paper are available from the corresponding authors upon request.

Code availability

Source codes for the ab initio model and Boltzmann transport equation calculation are available from the corresponding authors upon request.

References

36. Brown, A. M., Sundararaman, R., Narang, P., Goddard, W. A. & Atwater, H. A. Nonradiative plasmon decay and hot carrier dynamics: effects of phonons, surfaces, and geometry. *ACS Nano* **10**, 957–966 (2015).
37. Prineha, N., Ravishankar, S., Jermyn, A. S., Goddard, W. A. & Atwater, H. A. Cubic nonlinearity driven up-conversion in high-field plasmonic hot carrier systems. *J. Phys. Chem. C* **120**, 21056–21062 (2016).
38. Garcia, C. A. C., Coulter, J. & Narang, P. Optoelectronic response of the type-I Weyl semimetals TaAs and NbAs from first principles. *Phys. Rev. Res.* **2**, 013073 (2020).
39. Ciccarino, C. J., Christensen, T., Sundararaman, R. & Narang, P. Dynamics and spin-valley locking effects in monolayer transition metal dichalcogenides. *Nano Lett.* **18**, 5709–5715 (2018).
40. Nam, Y., Ki, D.-K., Soler-Delgado, D. & Morpurgo, A. F. Electron–hole collision limited transport in charge-neutral bilayer graphene. *Nat. Phys.* **13**, 1207–1214 (2017).
41. Rahbar, S. & Hashemizadeh, E. A computational approach to the Fredholm integral equation of the second kind. In *Proc. World Congress on Engineering* Vol. 2 (eds Ao, S. I. et al.) 933–937 (Newswood, 2008).
42. Ali, M. N. et al. Correlation of crystal quality and extreme magnetoresistance of WTe_2. *Europhys. Lett.* **110**, 67002 (2015).
43. Luo, Y. et al. Hall effect in the extremely large magnetoresistance semimetal WTe_2. *Appl. Phys. Lett.* **107**, 182411 (2015).
44. Zhao, Y. et al. Anisotropic magnetotransport and exotic longitudinal linear magnetoresistance in WTe_2 crystals. *Phys. Rev. B* **92**, 041104 (2015).

Acknowledgements

We thank M. Ku and A. S. Jermyn for fruitful discussions. We also thank P. Gumann and R. Stöhr for the initial design and construction of the microscope. T.X.Z. thanks R. Walsworth and M. Turner for diamond-processing assistance. Funding: this work was primarily supported by ARO grant no. W911NF-17-1-0023 and the Gordon and Betty Moore Foundations EPiQS Initiative through grant no. GBMF4531. Fabrication of samples was supported by the US Department of Energy (DOE), Basic Energy Sciences Office, Division of Materials Sciences and Engineering, under award DE-SC0019300. A.Y. acknowledges support from ARO grants W911NF-18-1-0316 and W911NF-1-81-0206, NSF grant DMR-1708688, and the STC Center for Integrated Quantum Materials, NSF grant no. DMR-1231319, and the Aspen Center of Physics supported by NSF grant PHY-1607611. G.V., Y.W. and P.N. acknowledge support from the Army Research Office MURI (Ab-Initio Solid-State Quantum Materials) grant no. W911NF-18-1-0431, which supported the development of computational methods to describe the microscopic, temperature-dependent dynamics in low-dimensional materials. G.V. acknowledges support from the Office of Naval Research grant on High-T_c Superconductivity at Oxide–Chalcogenide Interfaces (grant no. N00014-18-1-2691), which supported the theoretical and computational methods for phonon-mediated interactions. Y.W. is partially supported by the STC Center for Integrated Quantum Materials, NSF grant no. DMR-1231319, for the development of computational methods for topological materials. This research used resources of the National Energy Research Scientific Computing Center, a DOE Office of Science User Facility supported by the Office of Science of the US Department of Energy under contract no. DE-AC02-05CH11231 as well as resources at the Research Computing Group at Harvard University. This work was performed, in part, at the Center for Nanoscale Systems (CNS), a member of the National Nanotechnology Infrastructure Network, which is supported by the NSF under award no. ECS-0335765. CNS is part of Harvard University. P.N. is a Moore Inventor Fellow and gratefully acknowledges support through grant no. GBMF8048 from the Gordon and Betty Moore Foundation. C.A.C.G. acknowledges support from the NSF Graduate Research Fellowship Program under grant no. DGE-1745303. A.T.P. acknowledges support from the Department of Defense (DOD) through the National Defense Science and Engineering Graduate Fellowship (NDSEG) Program.

Author contributions

J.G., P.N. and A.Y. conceived the project. U.V., A.H., T.X.Z. and Y.D. designed and developed the experimental setup under the guidance of A.Y. N.K. and J.G. grew the bulk WTe_2 crystals under the guidance of C.F. U.V., A.H., Z.Q. and A.T.P fabricated and characterized the WTe_2 flakes. G.V. implemented the numerical BTE methods under the guidance of P.A. and P.N. G.V., Y.W. and C.A.C.G. developed and implemented the ab initio theoretical methods under the guidance of P.N. U.V., A.H., G.V., Y.W., P.N. and A.Y. analysed the data and discussed the results. All the authors contributed to the writing of the manuscript.

Competing interests

The authors declare no competing interests.

Additional information

Extended data is available for this paper at https://doi.org/10.1038/s41567-021-01341-w.

Supplementary information The online version contains supplementary material available at https://doi.org/10.1038/s41567-021-01341-w.

Correspondence and requests for materials should be addressed to Georgios Varnavides, Prineha Narang or Amir Yacoby.

Peer review information *Nature Physics* thanks Sergey Dushenko and the other, anonymous, reviewer(s) for their contribution to the peer review of this work.

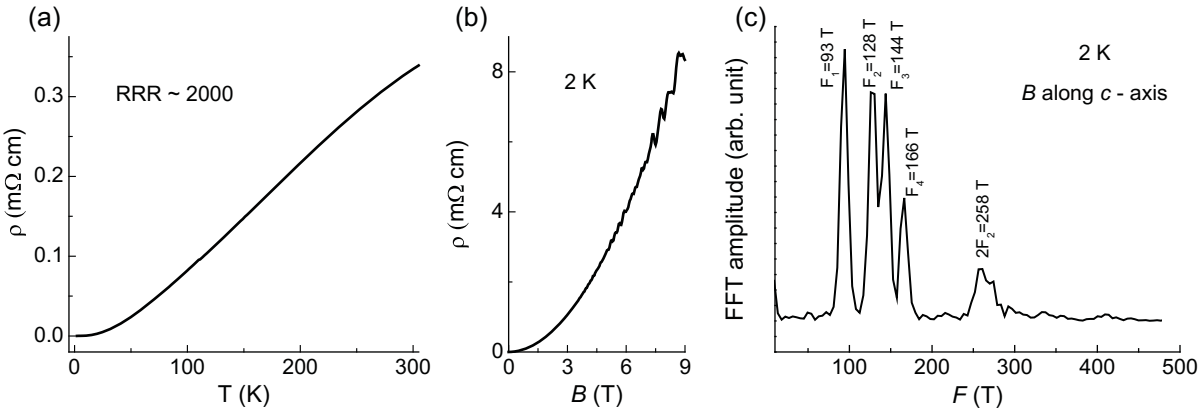

Extended Data Fig. 1 | Residual resistivity ratio and quantum oscillations. a, Temperature dependent resistivity at zero magnetic field. The residual resistivity ratio (RRR) between 300 Kand 2 K is approximately 2000, signifying the high quality of the single crystal. **b**, Magnetic field (applied along the ĉ-axis) dependent resistivity showing Shubnikov-de Haas oscillations at 2 K. **c**, The fast Fourier transform (FFT) of the background-subtracted data of (b) when plotted against the inverse of the magnetic field. We notice four fundamental peaks corresponding to the extremal orbits of the electron and hole pockets in the Brillouin zone[24].

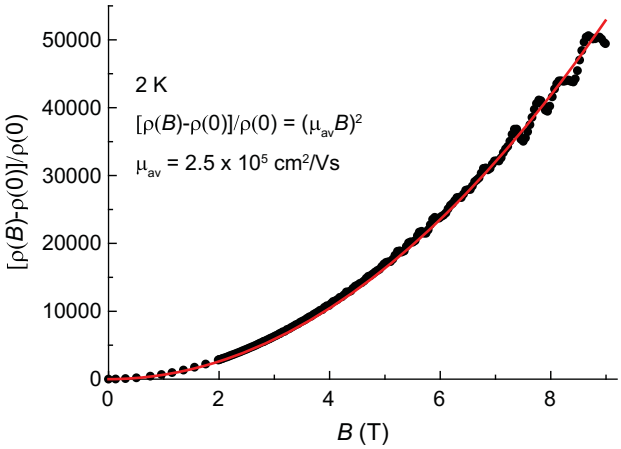

Extended Data Fig. 2 | Magnetic field dependent resistivity. Fitting of the magnetic field dependent resistivity at 2 K according to the relation $\frac{\rho(B)-\rho(0)}{\rho(0)} = (\mu_{av}B)^2$ where μ_{av} is the average mobility[24,42]. This allows us to extract $\mu_{av} = 2.5\times10^5 \mathrm{cm}^2/\mathrm{Vs}$. Using the relation $\sigma = \mu ne$, the average carrier density $n = 1.47\times10^{20}\,\mathrm{cm}^{-3}$ can be extracted.

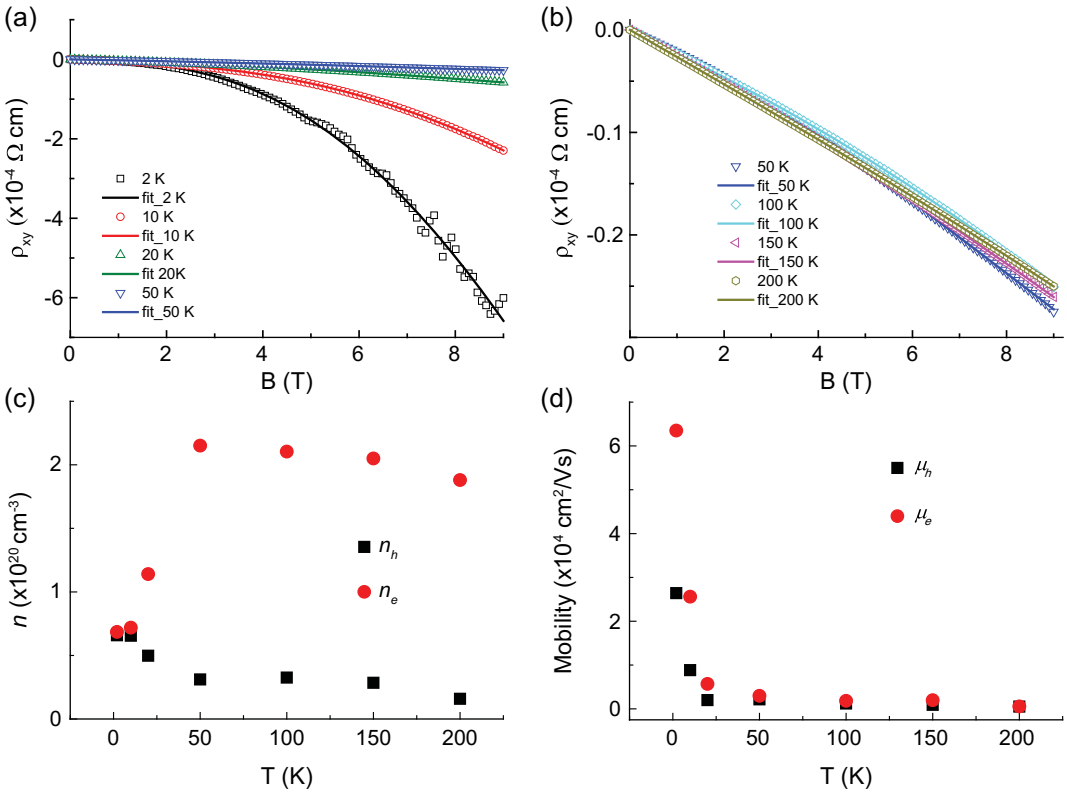

Extended Data Fig. 3 | Hall resistivity fitted to the two-band model. a, **b**, Hall resistivity vs. magnetic field measured at different temperatures. The data is fitted according to the two band model $\rho_{xy} = \frac{B}{e}\frac{(n_h\mu_h^2 - n_e\mu_e^2) + (n_h - n_e)\mu_h^2\mu_e^2B^2}{(n_h\mu_h + n_e\mu_e)^2 + (n_h - n_e)^2\mu_h^2\mu_e^2B^2}$ [43,44]. **c**, Carrier density of electrons and holes vs. temperature, extracted from the fits in (a) and (b). **d**, Mobility of electrons and holes vs. temperature, extracted from the fits in (a) and (b).

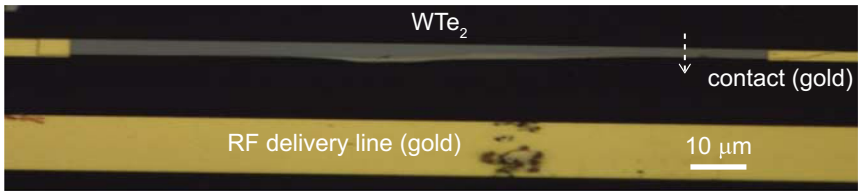

Extended Data Fig. 4 | WTe2 device. Optical image of the WTe_2 sample used for the majority of the data in the manuscript, including Main text Fig. 2, 3, and 4. The 100 μm long flake is contacted at its ends with gold contacts. The path along which our magnetic field profiles were taken is shown in white. An additional gold line nearby is used for delivery of RF power to manipulate the NV.

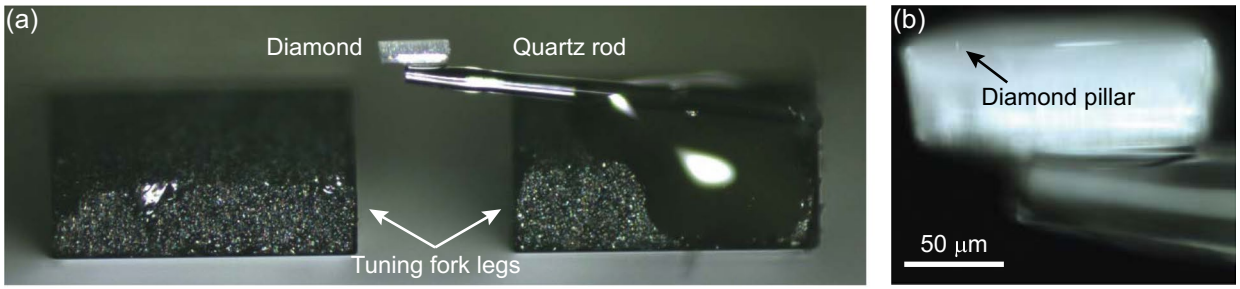

Extended Data Fig. 5 | Diamond scanning probe. a, An optical image of our scanning tip. A quartz rod is glued to the edge of one of the prongs of a quartz tuning fork. A diamond cube of $50 \times 50 \times 125\,\mu$m is glued to the other side of the rod. **b**, A closeup image of the diamond cube, with a 3 μm etched pillar visible. This pillar is used as our scanning probe, and an NV defect is located approximately 20 nm away from the pillar edge.

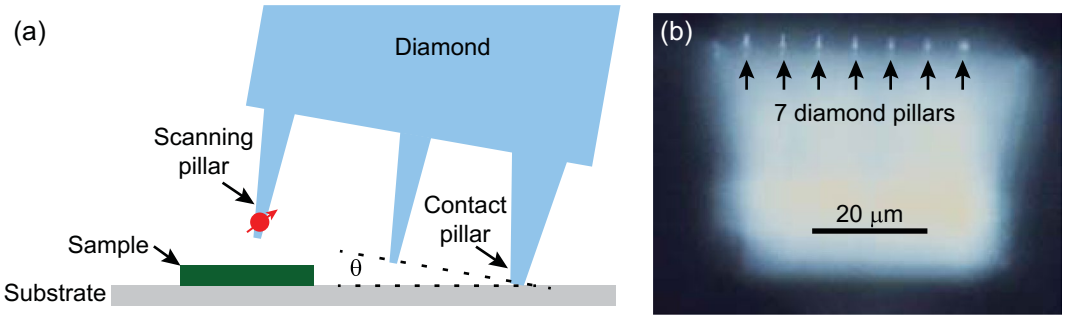

Extended Data Fig. 6 | Multiple pillar sensing. a, A schematic for multiple pillar sensing. The diamond is tilted at an angle θ (using goniometric motors) so that one pillar is in contact with the substrate, while the scanning pillar maintains a constant height above the sample without touching it. The angle θ controls the height of the NV probe above the sample. **b**, An optical image of a multiple pillar scanning tip with 7 pillars. The extreme pillars are made to be thicker so they are optimized for durability in contact, while the central pillars are optimized for NV sensing.